Chinese Journal of Chemical Engineering 82 (2025) 281–293

Contents lists available at ScienceDirect

Chinese Journal of Chemical Engineering

journal homepage: www.elsevier.com/locate/CJChE

Full Length Article

Magnetite-based pumice silica nanocomposite for lead adsorption from aqueous solution: The green synthesis approach

Genet Tsegaye [1,4], Zebene Kiflie [1,*], Jemal Fito Nure [2], Abera D. Ambaye [3,4]

[1] School of Chemical and Biochemical Engineering, Addis Ababa Institute of Technology, Addis Ababa University, Addis Ababa 1176, Ethiopia
[2] School of Chemical and Metallurgical Engineering, University of the Witwatersrand, 1 Jorissen St, Johannesburg 2000, South Africa
[3] Department of Chemical and Materials Engineering, University of South Africa, Private Bag X6, Florida Gauteng 1709, South Africa
[4] Bio and Emerging Technology Institute Addis Ababa 5954, Ethiopia

ARTICLE INFO

Article history:
Received 4 October 2024
Received in revised form
1 January 2025
Accepted 24 January 2025
Available online 17 March 2025

Keywords:
Adsorbent
Toxic metal
Nanomaterial
Bio-based
Phyto-fabrication
Water treatment

ABSTRACT

Lead (Pb) is a toxic metal found in wastewater, posing significant health risks to both humans and the environment. This study aimed to develop a novel adsorbent for lead removal from aqueous solutions. This adsorbent, a coffee husk extract-capped magnetite with pumice silica nanocomposite (CHE-capped M/PU/Si-NC), was synthesized using a completely green approach. The novelty of this study lies in the green synthesis of silica nanoparticles (SiO_2-NPs) throughout the process. Coffee husk extract (CHE) served as both a stabilizing and capping agent for the SiO_2-NPs, which were synthesized from sodium silicate (Na_2SiO_3) extracted from bagasse ash (BA). Subsequently, the CHE-capped silica was co-precipitated with phyto-fabricated magnetite and integrated into a pumice matrix to produce the final CHE-capped M/PU/Si-NC adsorbent. The CHE-capped M/PU/Si-NC was characterized using SEM, XRF, FTIR, BET, XRD, TGA, and zeta potential analysis. The surface area of the CHE-capped M/PU/Si-NC was determined to be 313 $m^2 \cdot g^{-1}$, and TGA results indicated good thermal stability up to 690 °C. The zeta potential was measured at −37.7 mV. XRD analysis of CHE-capped M/PU/Si-NC confirmed the formation of magnetite and revealed its crystal structure. The maximum adsorption performance of this material was observed to be 95% at an adsorbent dosage of 2 $g \cdot L^{-1}$ and an initial Pb^{2+} concentration of 100 $g \cdot L^{-1}$. The adsorption kinetics were best described by the pseudo-second-order kinetic model. The Langmuir isotherm provided a good fit with a maximum adsorption capacity of 150 $mg \cdot g^{-1}$ ($R^2 = 0.99$). Regeneration studies demonstrated that the adsorbent maintained its high Pb^{2+} uptake capacity for up to five cycles. Overall, these findings suggest that this adsorbent is a promising candidate for the removal of Pb^{2+} from water and wastewater.

1. Introduction

Heavy metals pose serious problems due to their toxicity and are categorized as the most dangerous pollutants to the environment [1]. In addition, most toxic metals can adversely impact the health of humans and animals [2]. Although heavy metals serve as valuable inputs for numerous industries, their direct release into the environment results in their buildup in soil and water. Subsequently, during irrigation and agricultural activities, these metals can readily accumulate in the human body. Lead, a toxic heavy metal, originates from both natural and human activities. Natural sources include lead-containing minerals in the Earth's crust, while anthropogenic sources encompass mining, smelting, industrial processes, lead-based paints, water distribution systems, vehicle emissions, and improper recycling and waste disposal. Lead pollution poses serious health risks, especially to children, causing neurological damage, developmental issues, and other health problems. Efforts to mitigate lead contamination involve regulations, the banning of lead-based products, improved waste management, and lead-safe practices in various industries. Nevertheless, the removal of lead from aquatic ecosystems stands as a significant global concern [3].

Recent technologies have been used for the removal of heavy metals including ion exchange resins [4], electrocoagulation and electrochemical depositions [5], nanofiltration, and reverse osmosis [6,7]. However, these methods have still some gaps that need to be addressed to further improve their efficiency and effectiveness. Recently, the development of advanced adsorbent

* Corresponding author.
E-mail addresses: kifliez@gmail.com, zebene.kiflie@aau.edu.et (Z. Kiflie).

https://doi.org/10.1016/j.cjche.2025.01.013

materials for heavy metal removal has gotten significant attention in the field of water treatment [8]. An effective water treatment mechanism is nanotechnology which utilizes engineered nanoparticle (NPs) and nanomaterials to clean up polluted water [9]. Nanoparticle-based technologies are often cost-effective compared to other technologies [10]. This is because NPs can be easily synthesized using low-cost precursors and the synthesizing process can be scaled up for high performance in industrial applications [11]. Furthermore, nano adsorbents can be regenerated and reused multiple times, thus reducing the amount of waste generated during the treatment process [12]. Several studies have shown that nanomaterials such as iron oxide, titanium dioxide, and carbon nanotubes can effectively be used to remove heavy metals including lead, chromium, and cadmium [13]. Silica NPs have shown great potential in adsorbing heavy metals due to their large surface area, high adsorption capacity, and tunable surface properties compared to other NPs [14]. However, there are still several gaps and challenges that exist in utilizing silica NPs for heavy metals adsorption.

Silica NPs often exhibit rapid adsorption kinetics at the initial stage but the rate of adsorption decreases over time as the NPs become saturated. Understanding and optimizing the kinetics of heavy metal adsorption on silica NPs is an area that requires further investigation [15]. Moreover, silica NPs tend to form agglomerates in aqueous environments. Developing strategies to enhance the stability of silica NPs and prevent aggregation is crucial for improving their performance in heavy metal adsorption [16]. The other drawback is related to the regeneration and reusability of silica NPs for heavy metal adsorption. Developing effective regeneration techniques and understanding the long-term stability and performance of silica NPs during multiple adsorption-desorption cycles is, therefore, important [17]. So far, several studies have been carried out on the incorporation of magnetite with silica for heavy metal removal: silica-coated magnetic nanocomposites for Pb^{2+} removal from aqueous solution [18], silica-coated $Cu_{0.50}Mg_{0.50}Fe_2O_4$ magnetic adsorbent for wastewater treatment [14], magnetic mesoporous silica microspheres with accessible carboxyl functionalized surfaces for the removal of heavy metal ions [19], magnetic silica-based hybrid organic–inorganic nanocomposite for the removal of lead (II) and nickel (II) ions from aqueous solutions [20] and network–polymer–modified superparamagnetic magnetic silica NPs for the adsorption and regeneration of heavy metal ions [21]. All aforementioned studies employed synthesis mechanisms based on chemical methods, such as the sol–gel method, Stöber method, flame synthesis, and microemulsion. While these chemical approaches are relatively straightforward to implement and modify, they can be expensive, energy-intensive, environmentally unfriendly, and difficult to control. Conversely, green synthesis of metallic NPs involves synthesizing NPs using natural sources or biodegradable agents, providing eco-friendly and sustainable alternatives to conventional methods [22]. The green synthesis approach uses natural reducing and stabilizing agents extracted from plants, algae, fungi, bacteria, and yeasts to form metal NPs [23,24].

This study has attempted to address the gap in the synthesis of silica nanoparticles (SiO_2-NPs) from agricultural residue as a silica precursor reported in the literature [17,18,25–31]. All aforementioned studies utilized green synthesis in the first stage to produce sodium silicate (Na_2SiO_3), followed by chemical synthesis in the second (final) stage to produce SiO_2 NPs. The novelty of this study lies in its utilization of green synthesis to manufacture SiO_2-NPs directly from their first product (Na_2SiO_3), thus completing the approach entirely using green synthesis. This investigation is a continuation of our ongoing research in the green synthesis of NPs by employing coffee husk extract (CHE) phenolic compounds as reducing and stabilizing agents for silica NPs in sodium silicate (Na_2SiO_3). This approach eliminated the need for chemical surfactants, resulting in the production of novel CHE-capped silica NPs. In addition, the present study has aimed to identify the key differences between CHE-capped silica NPs synthesized using this method and those produced through conventional sol-gel methods.

Although prior studies have investigated the use of combinations of magnetic materials and silica NPs for lead adsorption [32–34], none have previously coupled them with phytochemically generated silica NPs and magnetite incorporated into pumice (PCI). Pumice, a naturally abundant and cost-effective volcanic rock, possesses a high surface area for adsorption due to its porous nature [35,36]. Moreover, the addition of magnetic components renders the plant-mediated nanocomposite (NC) magnetically responsive, enabling easy separation and recovery from water. Green-synthesized magnetic silica NCs have emerged as a promising solution for the adsorption of lead ions from water. This study also determined the optimal lead adsorption parameters values using the synthesized NC. In general, our study developed a novel, green, and efficient adsorbent for lead removal from water by synthesizing a plant-mediated magnetite-based pumice silica NC. The significance of this study relies in its relevance to advancing research in NP synthesis, the synthesis of bio-based surfactants, and green approaches to remediate environmental pollution.

2. Materials and Methods

2.1. Materials

Lead nitrate ($Pb(NO_3)_2$), ferric chloride ($FeCl_3$, 99%), ferrous sulfate ($FeSO_4 \cdot 7H_2O$, 99%), ethanol (C_2H_5H, 99.02%), and ammonium hydroxide (NH_4OH) were purchased from Loba Chemie Pvt. Ltd. Coffee husk (CH) was gathered from Harer, Ethiopia. Volcanic pumice was collected from the Adulala pumice area, Bishoftu District, Ethiopia. Bagasse ash (BA) was obtained from the Wonji sugar factory in Ethiopia.

2.2. Silica nanoparticle synthesis

Sodium silicate was primarily extracted from HCl acid pretreated [37] BA by melting a mixture of sodium hydroxide and HCl pretreated ash at 550 °C for 1 h at a mass ratio of 1:1.5. After cooling to room temperature, distilled water was added to the mixture and refluxed (at boiling point) for 4 h to dissolve all of the sodium silicate, which was then used to synthesize silica [30]. Silica NPs were synthesized using both chemical (sol–gel) and green synthesis techniques. Sol–gel SiO_2-NPs were prepared by adjusting sodium silicate to pH 9 with 2.5 $mol \cdot L^{-1}$ HCl and aging it at room temperature for 24 h [29]. After filtering, sol–gel silica (Sol-Si) was washed with hot water and dried at 100 °C for 5 h. Silica NPs synthesized through a green (plant-mediated) approach were also produced following the modified method of Rahimzadeh *et al.* [32]. The filtrate Na_2SiO_3 and CHE were mixed and stirred at 60 °C in a 2:1 vol ratio. The procedure was carried out under reflux for 12 h at pH 9. After centrifugation at 7000 $r \cdot min^{-1}$ for 25 min, the precipitate was carefully washed with double distilled water three times and with ethanol as well. The CHE-capped SiO_2 NPs (CHE-Si) were then heated in a furnace at 550 °C for 45 min for removal of the contaminants and organic elements. Then, the residue was dried in an oven and kept for further characterization and application activities.

2.3. Preparation of CHE capped M/PU/Si NC

CHE-capped magnetite (M)/PU/Si-NC was synthesized by first preparing a magnetite pumice NC solution using a method adapted

from our previous work [38]. Pumice was initially washed, dried in an oven, ground, sieved, and acid-pretreated with HCl to remove metallic impurities and rinsed with deionized water until a neutral pH was achieved [39]. It was then dispersed in deionized water and sonicated. As illustrated in Fig. 1, iron salt precursors (ferrous sulfate and ferric chloride) were subsequently added and thoroughly mixed using a magnetic stirrer until 80 °C was reached. CHE was then introduced and mixed for 5 min, followed by the dropwise addition of ammonia until the pH reached 9.0. This process resulted in the formation of a black-colored CHE-capped Fe_3O_4/PU-NC, which was cooled to room temperature after 30 min of continuous stirring. The precipitate was separated using an external ferrite magnet and washed repeatedly with deionized water. Finally, the product was dried in an oven at 80 °C for 24 h. Then, CHE-capped M/PU/Si-NC was synthesized by slowly dropping the magnetic pumice solution into the nano-silica solution with continuous mixing for 2 h, after which the solution was centrifuged (Fig. 1) and dried in an oven at 80 °C for 3 h [40].

2.4. Adsorbent characterization

X-ray fluorescence spectrometers (PANalytical Epsilon 3, XRF, Monterrey, México) were used for the analysis of the oxide composition of BA. XRD (Bruker D8 Advance, Germany) was employed to better understand the behaviors of the synthesized material and confirmation of silica and CHE-capped M/PU/Si NC formation. FTIR spectra were used (IR Prestige, 21 Shimadzu, Japan) to determine the functional groups present in synthesized materials in the 400–4000 cm^{-1} range. Zeta potential analysis (Zeta-potential Nano series, Malvern, Westborough, MA, USA) was performed to determine the stability and surface charge while BET analysis (SA-9600 Series Surface Area Analyzer, Horiba, Japan) was carried out for the surface area, pore volume, and pore size determination. The thermal stability and degradation behavior of the synthesized materials were characterized using thermogravimetric analysis (TGA, HCT-1, China) in a temperature range of 30°C to 900 °C (20 °C·min^{-1}). SEM with EDX (JCM-6000, PLUS, Japan) was employed to study the formation and morphology of CHE-capped M/PU/Si NC and also for surface elemental analysis, respectively [17,41].

2.5. Adsorption experiment

The adsorption process was investigated under the effects of dose (0.1–0.6 g), contact time (10–150 min), pH (2–9), and concentration (1–250 mg·L^{-1}) for lead removal using CHE-capped M/PU/Si-NC. All batch adsorption experiments were carried out in 100 ml rubber-stopped volumetric flasks. The flasks were placed inside an incubator shaker (Excella E24R) and shaken at 200 r·min^{-1} for the specified times. At the end of the specified times, the CHE-capped M/PU/Si-NC were separated and the remaining metal ion concentration in the solutions was determined using an atomic absorption spectrophotometer (mol·L^{-1} AA-7000). The pH of the solutions was kept stable by adding 0.1 mol·L^{-1} of HCl and NaOH solution as needed. The highest lead adsorption capacities were chosen as the optimal condition, and that value was applied to the next affecting factor of the study. The removal efficiency (R%) and adsorption capacities (q_t, q_e) of the CHE-capped M/PU/Si-NC for Pb^{2+} removal were calculated using Eqs. (1)–(3).

$$R = (C_0 - C_e) \times 100/C_0 \quad (1)$$

$$q_t = (C_0 - C_t) \times V/m \quad (2)$$

$$q_e = (C_0 - C_e) \times V/m \quad (3)$$

where q_t and q_e are the amounts of Pb^{2+} adsorbed at time t and at equilibrium (mg·g^{-1}), respectively. C_0, C_t, and C_e are concentrations of Pb^{2+} (mg·L^{-1}) at time 0, t, and equilibrium, respectively. V is the

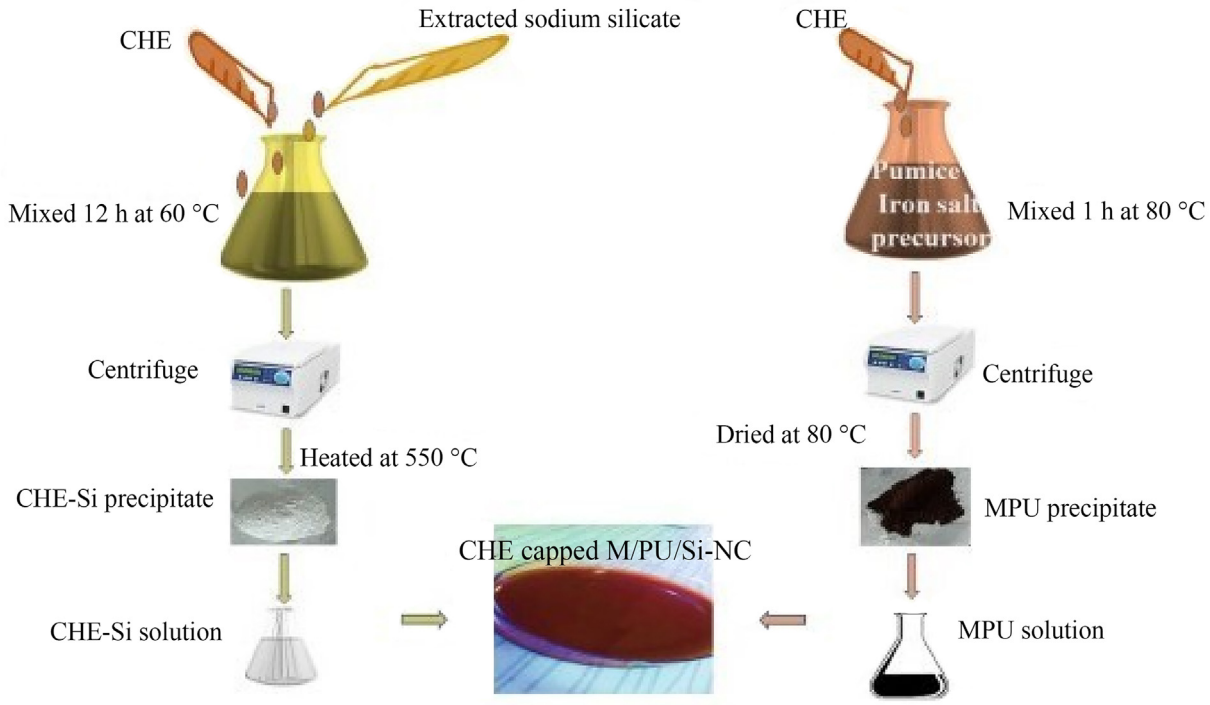

Fig. 1. Schematic illustration of the synthesis of CHE capped M/PU/Si NC.

volume of Pb^{2+} solution used (L) and m is the mass of adsorbent dosage that was used (g).

2.6. Adsorption kinetics

Adsorption kinetics models are frequently used to examine adsorption rate and rate-determining steps [15]. Pseudo-first-order (PFO), pseudo-second-order (PSO) models, and intraparticle diffusion (IPD) were used to understand the adsorption process of CHE-capped M/PU/Si-NC adsorbent. The pseudo-first-order model describes the physisorption limits of the adsorption rate of the particles onto the adsorbent. The non-linear form of the PFO model adsorbent capacity-based rate expression is given by Eq. (4) [42].

$$q_t = q_e\left(1 - e^{-k_1 t}\right) \tag{4}$$

where k_1 (min^{-1}) is the PFO rate constant, q_e ($mg \cdot g^{-1}$) and q_t ($mg \cdot g^{-1}$) are the amounts of Pb^{2+} adsorbed at equilibrium and at time t (min), respectively [43]. However, the PSO kinetic model describes the adsorption processes achieved *via* the chemical binding of adsorbates onto the surface of adsorbents. This kinetic model is expressed as:

$$q_t = q_e{}^2 k_2 t \Big/ (1 + q_e k_2 t) \tag{5}$$

where k_2 denotes the PSO equilibrium rate constant ($g \cdot mg^{-1} \cdot min^{-1}$). The other one is the IPD model which is the rate-limiting steps in the overall adsorption process if the line passes through the origin. The IPD model is expressed by Eq. (6).

$$q_t = K_{id}\, t^{1/2} + C \tag{6}$$

where K_{id} is IPD rate constant ($g \cdot mg^{-1} \cdot min^{-1}$) and q_t ($mg \cdot g^{-1}$) is the amount of lead ion adsorbed at any time t.

2.7. Adsorption isotherms

Adsorption isotherm models were used to study the effect of lead adsorbed from lead concentration per unit mass of CHE-capped M/PU/Si-NC adsorbent. The models can give important insights into the adsorption mechanism [44,45]. Langmuir, Freundlich, and Temkin models were used to identify the mechanism of Pb^{2+} adsorption onto CHE-capped M/PU/Si-NC adsorbent. The Langmuir adsorption isotherm describes non-interactive monolayer adsorption on a limited homogeneous surface [46]. The equilibrium correlation of Pb^{2+} and CHE-capped M/PU/Si-NC adsorbent is explained by the non-linearized Eq. (7).

$$q_e = Q_m K_L C_e / (1 + K_L C_e) \tag{7}$$

where q_e is the amount of adsorbed lead (mg) per g of adsorbent at equilibrium ($mg \cdot g^{-1}$), Q_m ($mg \cdot g^{-1}$) is the maximum adsorption capacity of the system ($mg \cdot g^{-1}$) and C_e is the adsorbate concentration in solution at equilibrium ($mg \cdot L^{-1}$), K_L is the Langmuir model constant. In contrast, the Freundlich isotherm describes multilayer adsorption at heterogeneous sites. Adsorption affinity and energy vary between adsorbent surfaces. Stronger binding sites are occupied first and binding strength decreases as site occupancy increases. The non-linear form of this model is described by Eq. (8).

$$q_e = K_f C_e^{1/n_f} \tag{8}$$

K_f and n_f are specific constants that correspond to the adsorbent's relative adsorption capacity and the intensity of adsorption, respectively [47]. Likewise, the Temkin isotherm model accounts for the indirect interactions between adsorbates and adsorbents. Essentially, it posits that as the surface coverage of the adsorbent increases, there will be a uniform decrease in the adsorption heat for all molecules on that surface [48]. The Temkin isotherm can be expressed by Eq. (9).

$$q_e = B \ln (A_T C_e) \tag{9}$$

where A_T is the Temkin equilibrium binding constant, B is the constant related to the heat of adsorption ($B = R_T/b_T$), R is the universal gas constant (8.314 $J \cdot mol^{-1} \cdot K^{-1}$).

3. Results and Discussion

3.1. Characteristics of the adsorbent

3.1.1. X-ray fluorescence (XRF) analysis

XRF analysis was conducted to study the oxide composition of BA which was used as a silica source. The XRF analyses show that the oxide compositions of BA were SiO_2 (65.8%), Fe_2O_3 (7.3%), Al_2O_3 (13.0%), and K_2O (8.6%) with a small LOI value of 1.6% which is similar to other studies [49,50]. Interestingly, acid pre-treatment significantly altered the oxide composition of BA. Silicon dioxide (SiO_2) became the dominant component, increasing to 85.8%. Conversely, the content of metal oxides like Fe_2O_3, aluminum Al_2O_3, and K_2O all decreased to 3.3%, 7.0%, and 4.0%, respectively. This reduction in metallic impurities may be attributed to the effective leaching action of hydrochloric acid [37,50]. These findings confirm that BA has a high content of SiO_2, making it a promising precursor for silica production [51,52].

3.1.2. FTIR analysis

To investigate the functional groups of the synthesized material and the role of phenolic compounds in their formation, Fourier-transform infrared spectroscopy (FTIR) analysis was performed on both the raw BA and the synthesized material. Fig. 2(a) shows the FTIR spectra of the BA. The BA spectra exhibit vibrational bands at 983, 788, and 430 cm^{-1}. These peaks correspond to asymmetric and symmetric stretching vibrations of Si—O—Si (at 983 cm^{-1} and 788 cm^{-1}, respectively) [53]. Similarly, the Si—O bending was found at 430 cm^{-1} [54]. The strong intensity of the Si—O peak suggests a high content of silicon oxide in BA, which is consistent with the high silicon oxide percentage found in the XRF analysis [50,55]. Fig. 2(b) shows the functional groups present in CHE-Si-NPs, CHE-capped M/PU/Si-NCs, and Sol-Si-NPs. The FTIR spectra of CHE-capped M/PU/Si-NCs exhibit peaks at 3430, 1625, 1109, 808, 570, and 460 cm^{-1}. CHE-Si-NPs show peaks at 3430, 1625, 1109, 808, and 460 cm^{-1}, while Sol-Si-NPs exhibit peaks at 3430, 1625, 1036, 808, and 460 cm^{-1}. The FTIR spectra of the synthesized materials reveal four common peaks (Fig. 2(b)). The strong, broad peak at 3430 cm^{-1} in CHE-capped Si and CHE-capped Si M/PU/Si-NC corresponds to stretching vibrations of Si—O—H groups. This peak is characteristic of the OH groups present in the phenolic compounds of CHE, suggesting their contribution to the formation of silica and Fe_3O_4-NPs [56,57]. In contrast, the weak, broad peak at 3430 cm^{-1} observed in Sol-Si-NPs likely arises from surface water adsorption [17]. The second common peak at 1625 cm^{-1} originates from bending vibrations within the silanol groups (Si—OH) [58]. The third peak at 808 cm^{-1} signifies symmetric stretching of siloxane bonds (Si—O—Si) as reported in various studies [18,30,58]. Finally, the last common peak at 460 cm^{-1} represents the bending vibrations of Si—OH bonds [48]. Interestingly, CHE-Si-NPs and CHE-capped M/PU/Si-NCs exhibit additional strong narrow peaks at 1109 cm^{-1}. This peak indicates the presence of asymmetric siloxane bonds (Si—O—Si) and bending vibrations of functional groups [59]. In contrast, analysis of Sol-Si-

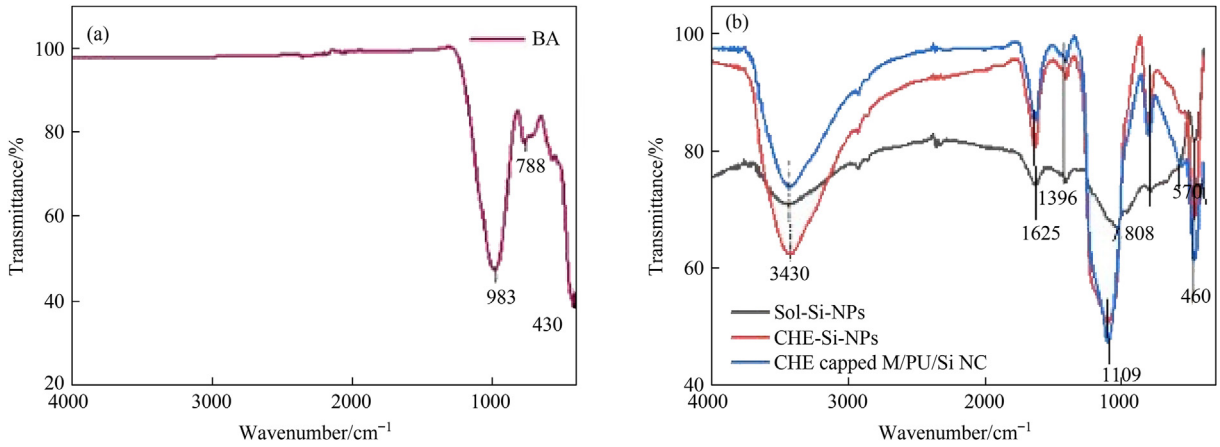

Fig. 2. FTIR spectra of (a) BA (b) Sol-Si-NPs, CHE-Si-NPs, and CHE capped M/PU/Si-NC.

NPs reveals a weak and broad peak at 1036 cm^{-1} which is associated with Si—O—Si asymmetric stretching vibrations [60]. This peak indicates a lower abundance of silica functional groups in the sample [61]. Furthermore, the FTIR spectra of CHE-capped M/PU/Si-NCs reveal an additional peak at 570 cm^{-1}. This peak is attributed to Fe—O—Si stretching vibrations within magnetite [17,18,62] and indicates the successful formation of Fe_3O_4 in the CHE-capped M/PU/Si-NC material. Generally, the FTIR analyses confirmed the phytochemicals present in the CHE acted as a reduction and capping agent in CHE-Si-NPs, and CHE-capped M/PU/Si-NCs.

3.1.3. X-ray diffractometer (XRD) analysis

The physical properties such as phase composition, crystal structure, and orientation of Sol-Si, CHE-Si, and CHE-capped M/PU/Si-NC which were investigated using the XRD are shown in Fig. 3. The broad peaks around 2θ=15°–30° in Fig. 3(a) and (b) confirm the presence of amorphous silica NPs in both samples synthesized using the plant-mediated and sol–gel methods, respectively [40,53,63]. Plant-mediated synthesis appears to yield SiO_2-NPs with less background noise compared to those produced by sol–gel synthesis. Notably, the diffraction peaks in both cases match the reference pattern for SiO_2 in JCPDS file No. 89—0510 [64]. Fig. 3(c) shows the XRD pattern of the CHE-capped M/PU/Si-NC. The pattern reveals

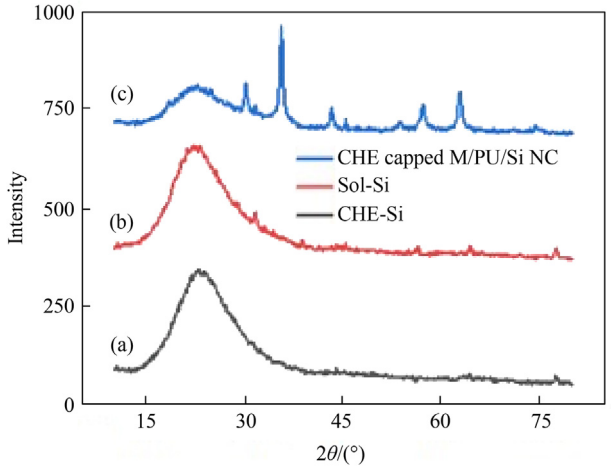

Fig. 3. XRD patterns of (a) CHE-Si-NPs, (b) Sol. Si-NPs, (c) CHE capped M/PU/Si-NC.

both crystalline and amorphous peaks. The crystalline peaks correspond to Fe_3O_4-NPs at 2θ values of 30.6°, 35.9°, 43.5°, 54.0°, 57.4°, 63.0°, and 74.5°. This observation is consistent with previous XRD results [17,40,65]. Additionally, a broad peak around 2θ=15°–30° indicates the presence of amorphous pumice [66] and silica NPs [67]. This XRD analysis confirms the formation of the composite material with a combination of crystalline Fe_3O_4 and amorphous SiO_2. Furthermore, the absence of impurity peaks in the entire pattern suggests high purity of the synthesized CHE-capped M/PU/Si-NC.

3.1.4. TGA and DTG analysis

TGA and DTG were used to evaluate and compare the thermal stability of Sol-Si, CHE-Si, and CHE capped M/PU/Si-NC are presented in Fig. 4(a) and (b). The relative comparison between weight losses of Sol-Si and that of CHE-Si is 6% at 129 °C and 3% at 250 °C, respectively. This condition is related to evaporation of physically and chemically adsorbed water. The second stage of decomposition observed in the range of CHE-Si from 250–650 °C with mass loss of 2.5% and Sol-Si 129–450 °C with mass loss of 3.5% was due to dehydration and evaporation of chemically adsorbed water molecules. This could also be associated with the removal of hydroxyl groups which is the surface dehydroxylation of silica [68]. This result confirms the successful synthesis of high thermally stable green capped silica NPs with high purity of silica (94.5%) at a higher temperature (650 °C) than Sol-Si NPs which is 89.7% purity at 463 °C. This is a very good indicator that the capping and stabilizing agents around the CHE-Si-NPs are strong enough to resist high temperatures [69]. The CHE-capped M/PU/Si-NC residue was 95% at the highest temperature (690 °C) [69]. Similar results have been found by other authors [63]. This revealed that the plant-mediated CHE-capped M/PU/Si-NC have better thermal stability compared to the bare silica NPs.

3.1.5. BET surface area determination

BET analysis was performed on microporous silica to assess its surface area and pore characteristics as shown in Table 1. The analysis revealed a surface area of 338 $m^2 \cdot g^{-1}$, a pore radius of 0.18 nm, and a pore volume of 0.079 $cm^3 \cdot g^{-1}$. This confirms the microporous nature of the synthesized material with pores predominantly less than 2 nm in size [70]. Compared to silica NPs synthesized using CTAB surfactant (323 $m^2 \cdot g^{-1}$), CHE-capped Si-NPs displayed superior surface area and pore characteristics [32]. Similarly, Sol-Si exhibited lower surface area (309 $m^2 \cdot g^{-1}$) and pore

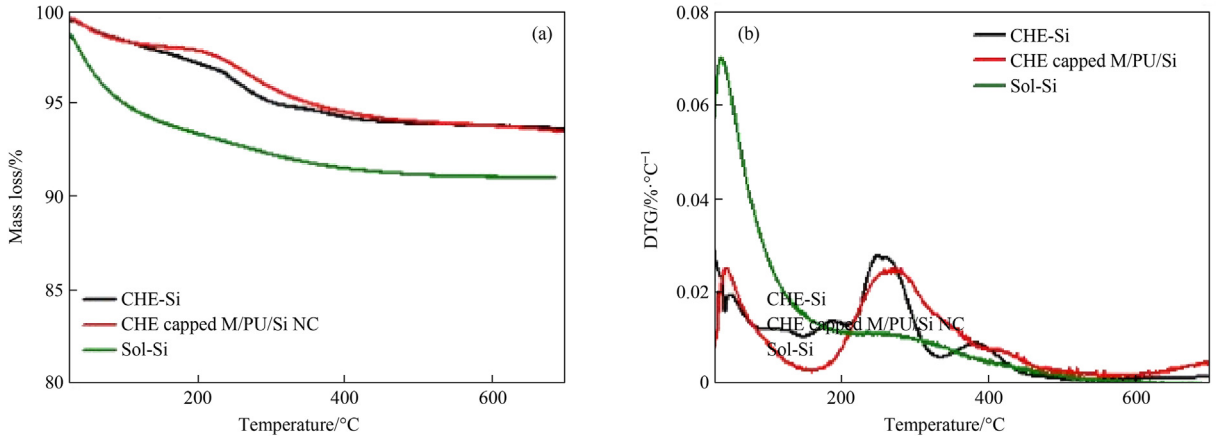

Fig. 4. (a). TGA curves of the synthesized Sol-Si, CHE-Si, and CHE capped M/PU/Si NC. (b) DTG curves of the synthesized Sol-Si, CHE-Si, and CHE capped M/PU/Si NC.

Table 1
N_2 adsorption-desorption analysis.

Name of nanomaterial	Surface area /$m^2 \cdot g^{-1}$	Pore volume /$cm \cdot g^{-1}$	Pore size /nm
Si-Sol gel	309	0.054	0.88
CHE-Si	338.1	0.079	0.18
CHE capped M/PU/Si NC	313.6	0.069	0.18

volume (0.05467 $cm^3 \cdot g^{-1}$) compared to CHE-capped silica. Furthermore, CHE-capped Fe_3O_4/PU/Si-NC possessed a surface area of 313.6 $m^2 \cdot g^{-1}$, pore volume of 0.069 $cm^3 \cdot g^{-1}$, and pore radius of 0.18 nm. This is significantly higher than the surface area of magnetic silica NCs (275 $m^2 \cdot g^{-1}$) and (172 $m^2 \cdot g^{-1}$) reported by Nicola *et al.* [18] and Faaliyan [71], respectively. These findings suggest that the use of phytochemical capping and stabilizing agents enhances both surface area and pore volume in CHE-capped M/PU/Si-NC and CHE-Si-NPs compared to Sol-Si NPs.

3.1.6. Zeta potential analysis

Zeta potential is an important parameter in evaluating CHE-capped M/PU/Si-NC stability and surface charge [72]. In this study, the zeta potential of CHE-capped M/PU/Si-NC surfaces was tested using the method used by Bakatula in solution at pH values of 2–10 [73]. The zeta potential of CHE capped M/PU/Si NC (Fig. 5) was negatively charged throughout the entire pH range but with increasing zeta potential charges from pH 2 to 6 due to increasing of SiO species [74,75] which became less negative when the pH of the aqueous solution increased from 7 to 10 which may be due to the repulsive forces occurring between the magnetite NPs and the negative charges of the basic medium [25]. Higher zeta potential charges were seen around pH 5 and 6 implying strong surface stability at this point and following optimal adsorption of positively charged lead ion (Fig. 5) on the surface of synthesized material due to the electrostatic attraction [42].

3.1.7. Scanning electron microscopy (SEM) analysis

SEM was employed to investigate the surface morphology of the CHE-capped M/PU/Si-NC before and after lead (Pb^{2+}) adsorption (Fig. 6). The pre-adsorption image (Fig. 6(a)) revealed spherical NPs, consistent with observations in other studies [17,26]. However, the morphology differed significantly after Pb^{2+} loading (Fig. 6(b)). The post-adsorption image displayed aggregates or clusters on the surface, suggesting the successful adsorption of Pb^{2+} ions. This highlights the crucial role of the microporous structure of the CHE-capped M/PU/Si-NC in Pb^{2+} capture from water as reported previously [76]. In essence, the SEM analysis confirms the well-established anionic and microporous nature of the NC surface which effectively attracts and adsorbs the cationic Pb^{2+} pollutant.

3.1.8. Energy dispersive spectroscopy (EDS) and EDS mapping analysis

An EDS study was conducted to prove unequivocally that the synthesized nanomaterial contains the anticipated elements. Fig. 7(a) shows that the elemental composition of CHE-capped Si includes Si and O, indicating that the NPs are silica [77]. According to the results, impurity elements such as Na and Cl are present because HCl and NaOH were used for pH adjustment, while the additional Au and C peaks were due to coating the sample during analysis. Furthermore, Fig. 7(b) shows that the chemical composition of CHE-capped M/PU/Si-NC exhibits peaks around 0.9 and 6.4 keV which corresponds to the Fe binding energies [78]. The oxygen peak at 0.5 keV and the Si peak at 1.8 keV confirm the presence of silica in the composite. The results are consistent with those reported by Rahman *et al.* [79]. The synthesized materials constituted about 100% of the identified elements, indicating high purity and free of extraneous impurities. The EDS elemental mappings of CHE-capped Si-NPs and

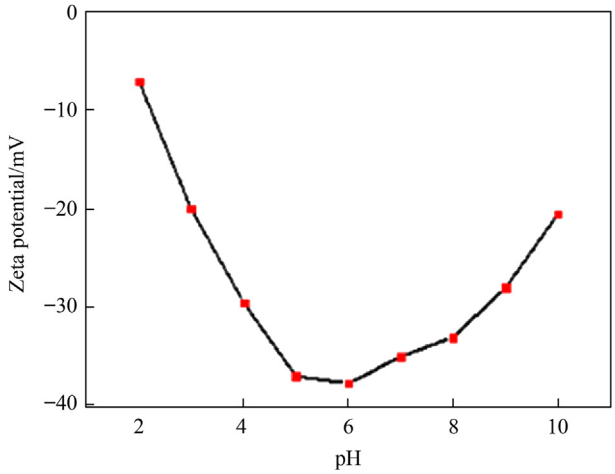

Fig. 5. Zeta potential *versus* pH for CHE capped M/PU/Si NC.

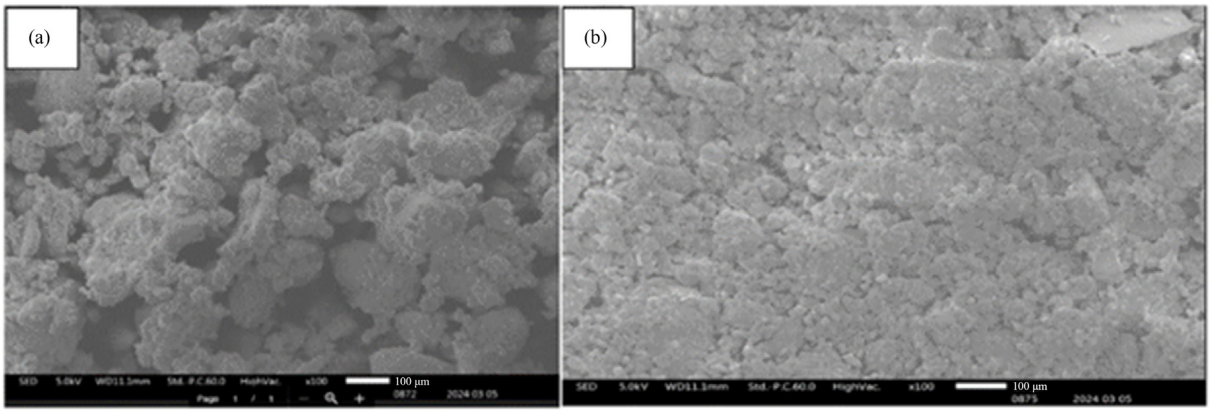

Fig. 6. SEM images of (a) CHE capped M/PU/Si-NC amd (b) CHE capped M/PU/Si-NC after Pb^{2+} absorption.

CHE-capped M/PU/Si-NC are presented in Fig 7(a) and (b). The CHE-capped Si EDS maps (Fig. 7(a)) show the purity of the synthesized CHE-capped Si NPs as well as the evenly distributed O and Si elements. The CHE-capped Fe_3O_4/PU/Si-NC EDS mapping (Fig. 7(b)) shows good homogeneity in the spatial dispersal of Fe, Si, O, Al, and O, showing that all elements are uniformly dispersed and that CHE-capped Fe_3O_4/PU/ZnO-NC was effectively phyto-fabricated.

3.2. Adsorption performances

3.2.1. Effect of pH

CHE-capped M/PU/Si-NC was used for lead ion adsorption, and it is crucial to identify the pH conditions that give the greatest adsorption capacity. As a result, this study investigated and demonstrated (Fig. 8) the impacts of starting solution pH on Pb^{2+} adsorption by CHE-capped M/PU/Si-NC in the pH range of 1–9. The graph indicates that the adsorption of Pb^{2+} increases with increasing solution pH up to a pH of 5. This is due to a reduction in the quantity of H^+ ions in the solution, which results in reduced competition [80]. Furthermore, as the pH increased, the negative charges of the adsorbent and active site increased, promoting electrostatic attraction complexation between the CHE-capped M/PU/Si-NC and Pb^{2+} [18]. Additionally, the ionization of functional groups, such as hydroxyl (—OH) and silanol (—SiOH), varies with pH. At pH 5, more hydroxyl groups may be deprotonated, increasing the availability of active sites for lead complexation and lead ion adsorption [81]. Even if the deprotonation of the CHE-capped M/PU/Si-NC was enhanced, the adsorption efficiency was

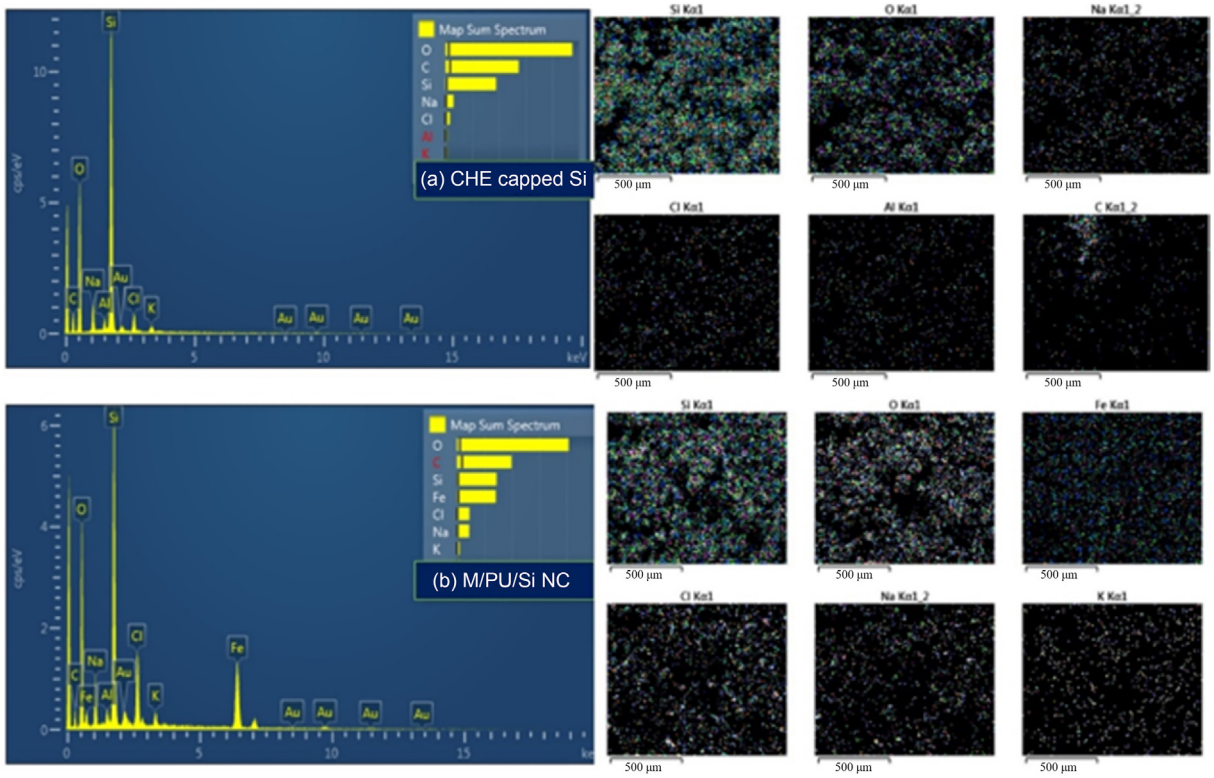

Fig. 7. Energy dispersive spectroscopy (EDS) and EDS mapping analysis of (a) CHE capped Si and (b) M/PU/Si NC.

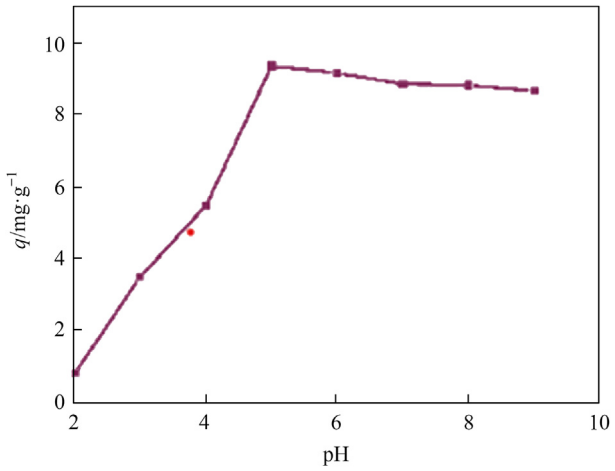

Fig. 8. Adsorption capacity of CHE-capped M/PU/Si-NC at different pH (adsorption conditions were, $t = 60$ min, $C_0 = 10$ mg·L^{-1}, agitation speed = 200 r·min^{-1}, $T = 25$ °C, adsorbent dose = 1 g·L^{-1}

observed to decrease above the pH of 5. This can be because lead ions may form insoluble hydroxides and precipitate, limiting their availability for adsorption [18]. As a result, an initial pH of 5 was selected as the best setting for the sorption of lead ions in the subsequent adsorption studies [80,82].

3.2.2. Effect of contact time

As shown in Fig. 9, lead ion adsorption increases initially until it reaches equilibrium at 60 min. This is due to the abundance of adsorption sites on NC which the lead ions can easily access and bind to. The adsorption capacity of the NC rises as more lead ions meet it. After 60 min, there is an approximately constant effect on adsorption, and lead ion adsorption achieves equilibrium. At this moment, the rate of adsorption equals the rate of desorption, resulting in the saturation of accessible adsorption sites on the NC surface [83]. At equilibrium, additional contact time does not result in considerable additional adsorption. Beyond 60 min, the adsorption capacity shows a limited reduction as well as a slight fall in adsorption capacity. This occurs due to the desorption of previously adsorbed lead ions due to the limited access to adsorption sites due to mass transfer restrictions [84].

3.2.3. Effect of adsorbent dose

To investigate the effect of CHE-capped M/PU/Si NC adsorbent dose on lead ion adsorption capacity and removal efficiency by varying the CHE-capped M/PU/Si NC dose from 1 to 6 g·L^{-1} while maintaining the other adsorption parameters constant. As illustrated in Fig. 10, the CHE-capped M/PU/Si NC adsorption capacity (q) reduced as the CHE-capped M/PU/Si NC dose increased. However, as the CHE-capped M/PU/Si NC dose increased from 0.1 to 2 g·L^{-1}, the removal (R) increased. The availability of more adsorption sites has been connected to increases in removal efficiency as the CHE-capped M/PU/Si NC increased. The higher the adsorbent dose, the more binding active sites were provided, and the metal ions had a higher probability of adsorption, resulting in increased removal of the metal ions from the solution. As the dose rose to 6 g·L^{-1}, the adsorption capacity declined while the removal efficiency remained nearly constant. This could be because Pb^{2+} occupied the pore space in the CHE-capped M/PU/Si NC, leaving the active sites, (—SiOH, —OH, and —COOH) saturated. Excess amounts of adsorbent can result in overcrowding of particles which can impede the mass transfer of the target compounds. Particle aggregation or dispersion may also occur at very high adsorbent dosages. Aggregation can result in the creation of bigger aggregates with lower adsorption effectiveness than individual particles. Dispersion occurs when adsorbent particles separate excessively, resulting in diminished adsorption capacity due to reduced contact with the target chemicals. Therefore, 2 g·L^{-1} of CHE capped M/PU/Si NC dose was chosen for further adsorption studies, considering both adsorption capacity and removal efficiency.

3.2.4. Initial concentration effect

As shown in Fig. 11, the removal efficiency (R_{eff}, %) of Pb^{2+} by the CHE-capped M/PU/Si-NC decreased with increasing concentration of both ions in the solution while the adsorption capacity (q) increased. Initially, the removal efficiency was 93.3% for Pb^{2+} at 50 mg·L^{-1} which decreased to 90% for Pb^{2+} when the initial concentration was increased to 100 mg·L^{-1}. The adsorption capacity of the CHE-capped M/PU/Si-NC increased sharply as the initial concentrations increased from 50 mg·L^{-1} to 100 mg·L^{-1}. This is because a higher concentration of lead ions means a greater number of target ions available for adsorption [85]. More lead ions can bind to the available adsorption sites on the NC surface, resulting in a higher adsorption capacity. The adsorption capacity was reduced beyond the 100 mg·L^{-1} concentration increment. This

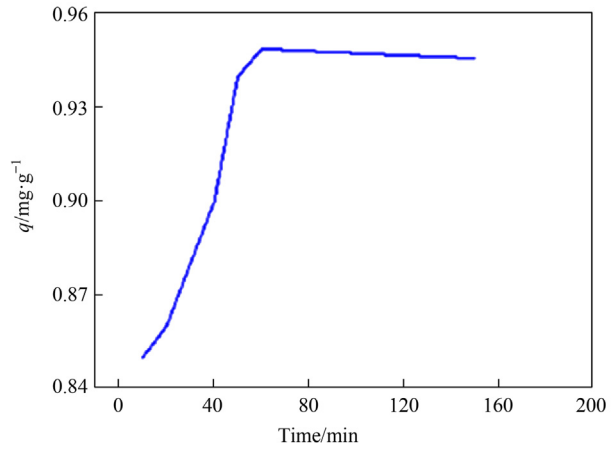

Fig. 9. Adsorption capacity of CHE-capped M/PU/Si NC at different contact times (adsorption conditions were pH=5, C_0=10 mg·L^{-1}, adsorbent dose=1 g·L^{-1}, agitation speed=200 r·min^{-1}, T=25 °C).

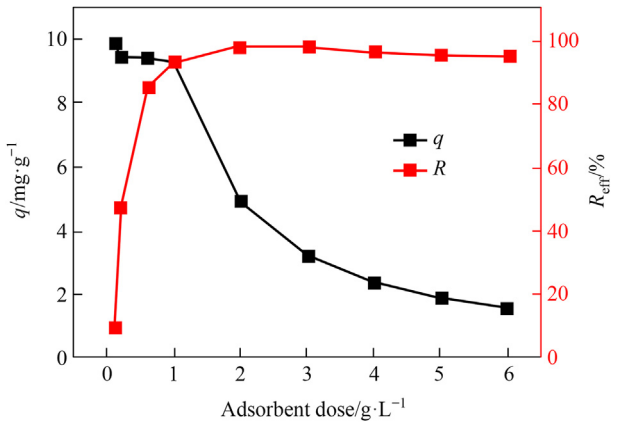

Fig. 10. Adsorption capacity of CHE-capped M/PU/Si-NC at different adsorbent doses (adsorption conditions were pH=2, C_0=10 mg·L^{-1}, t=60 min, agitation speed=200 r·min^{-1}, T=25 °C).

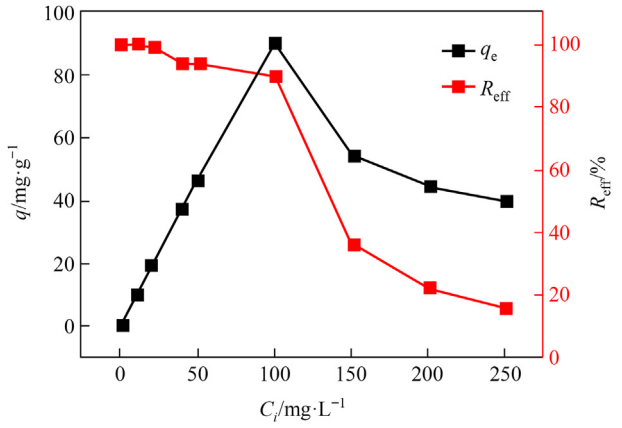

Fig. 11. Adsorption capacity of CHE-capped M/PU/Si-NC at different Pb^{2+} ions initial concentration (adsorption conditions were pH=5, t=60 min, adsorbent dose=2 g·L^{-1}, agitation speed=60 r·min^{-1}, T=25 °C).

may probably be because the adsorption capacity of the NC may reach saturation, even if the initial concentration of lead ions continues to increase. The saturation point corresponds to the maximum adsorption capacity that can be achieved for a given NC and concentration range. Beyond this point, increasing the initial concentration may not significantly enhance the adsorption efficiency or capacity. Also, this surface saturation occurs when all available adsorption sites are occupied by lead ions, and the NC is unable to adsorb additional lead ions. Thus, considering both adsorption capacity and removal efficiency, a concentration of 100 mg·L^{-1} was chosen for subsequent adsorption experiments.

3.3. Adsorption kinetics

PFO, PSO, and IPD kinetic models were studied to analyze the rate of adsorption of Pb^{2+} by CHE-capped M/PU/Si-NC beads. The adsorption kinetic models' results are presented in Table 2 and illustrated in Fig 12(a) and (b). As revealed in Table 2, the R^2 value of the PSO model (R^2=0.99) is higher than that of the PFO model (R^2=0.80). Similarly, q_{cal} for PSO (Table 2) better fits to q_{exp} than that of PFO. In many cases, the PSO model aligns well with the mechanism of adsorption onto CHE-capped M/PU/Si-NC. This result suggests that chemisorption is the predominant mechanism underlying the adsorption of lead ions and the adsorbent surface. This is often observed in the adsorption of heavy metal ions onto NCs where strong coordinate covalent bonds are formed between the metal ion (Pb^{2+}) and the surface functional groups (—SiOH, —OH, and —COOH) [86]. In addition, as shown in Table 2, the IPD model plot has a low regression coefficient (R^2=0.69) and the intercept is not equal to zero. Besides, one can observe that (Fig. 12(c)) the plot does not pass through the origin indicating that IPD was not the rate-limiting step and external diffusion might be involved in the process [87]. Therefore, the formation of the micropore structure of CHE-capped M/PU/Si-NC makes it easy for the diffusion of the lead ions to the active sites because of a microporous material successfully used for adsorbing heavy metals from water solutions [88].

Table 2
Summary of adsorption kinetic model parameters.

Kinetic model	Parameter	Pb^{2+}
Pseudo first order	q_{exp}/mg·g^{-1}	91.8
	q_{cal}/mg·g^{-1}	90.9
	R^2	0.80
	K_1	0.2681
Pseudo second order		
	q_{exp}/mg·g^{-1}	91.8
	q_{cal}/mg·g^{-1}	92.0
	R^2	0.99
	K_2	0.0128
Intra particle diffusion	C	86
	K_{diff}	0.522
	R^2	0.69

3.4. Adsorption isotherms

To investigate the relationship between initial Pb^{2+} concentration and Pb^{2+} uptake on CHE-capped M/PU/Si-NC adsorbents, Langmuir, Freundlich, and Temkin isotherm models were employed. The study was conducted at 25 °C for 60 min at a pH of 5. The initial Pb^{2+} concentration was varied from 1 to 100 mg·L^{-1} while maintaining a CHE-capped M/PU/Si-NC dose of 2 g·L^{-1}. Fig. 13(a) and (b) illustrate the non-linear fitting plots of the Langmuir, Freundlich, and Temkin isotherm models for Pb^{2+} adsorption onto CHE-capped M/PU/Si-NC. The adsorption isotherm parameters are presented in Table 3. Table 3 reveals that the Langmuir adsorption isotherm has a higher R^2 value (0.999) compared to Freundlich (0.991) and Temkin (0.977), indicating a better fit to the experimental data. The findings suggest that CHE-capped M/PU/Si-NC forms monolayer adsorption without interactions between adsorbed Pb^{2+} ions [46]. The maximum adsorption capacity (q_m) of the CHE-capped M/PU/Si-NC adsorbent for Pb^{2+} was found to be 151 mg·g^{-1}. A comparison of adsorption capacities of different magnetic silica-based adsorbents for Pb^{2+} removal is summarized in Table 3. Although the Freundlich model did not fit the data well, the empirical constant n value was greater than 1, suggesting a favorable adsorption process. This indicates a strong interaction between Pb^{2+} and the adsorbent surface [82]. Additionally, the Temkin adsorption isotherm's b_t value was very high (91.8 kJ·mol^{-1}), suggesting a strong heat of adsorption [48,89]. This implies the formation of strong attractive forces between the Pb^{2+} ions and the adsorbent surface, confirming the presence of chemisorption [90–92].

3.5. Comparison of the adsorption performances

An adsorbent's adsorption capacity is significantly influenced by its surface charge, surface area, and functional groups [93]. The surface charge also determines its stability, biocompatibility, and interactions with other molecules. Our CHE-mediated synthesized NC has good stable electrostatic properties and is negatively charged (−37 mV). This increases the adsorbent's electrostatic attraction to cationic pollutants. And also CHE/M/PU/Si-NC has a larger surface area (313.9 m^2·g^{-1}) than the earlier magnetic silica NC adsorbent [18]. Overall, the properties of CHE/M/PU/Si-NC suggest that it possesses a high adsorption capacity compared to other adsorbents. Table 4 presents a comparison of the maximum adsorption capacity (q_m) of our synthesized CHE-capped M/PU/Si-NC with values reported in the literature.

To understand the performance of adsorbents in real-world water samples, comparing their competitive adsorption behaviors is essential. Lead adsorption can be significantly influenced by the presence of other cations, such as cadmium and copper [96]. This study investigated the selectivity of CHE/M/PU/Si-NC for Pb^{2+} adsorption in solutions containing multiple ions. As depicted in Fig. 14, the adsorption efficiency for lead alone (control) was 97.5%. The addition of cadmium ions slightly reduced the adsorption efficiency to 97.35%, demonstrating a stronger competitive effect due to its smaller ionic radius and similar chemical properties [76]. While copper ions (97.45%) also competed with lead, their effect was generally less pronounced [97]. When all three ions were present, the combined effect on lead adsorption was greater than their individual effects (96.3%). Overall, CHE/M/PU/Si-NC remained effective in removing lead

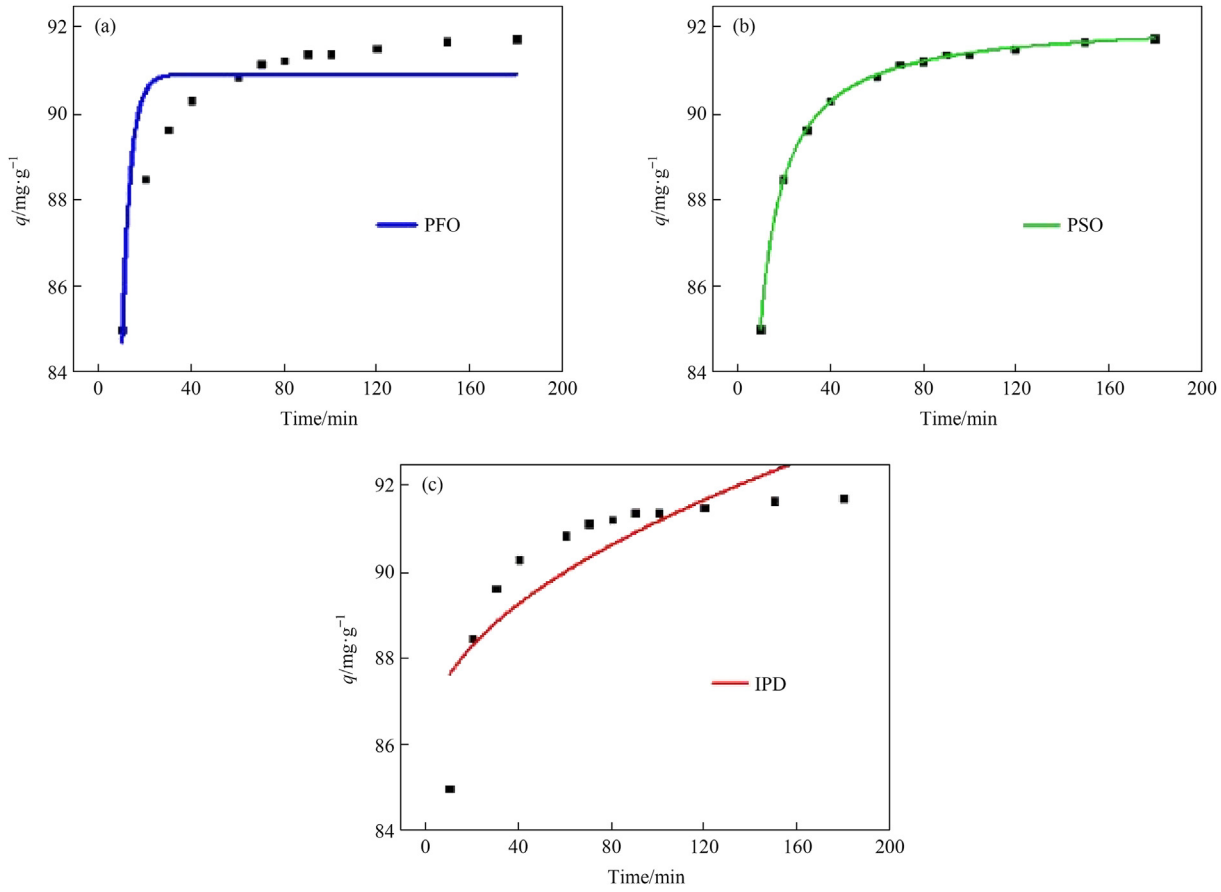

Fig. 12. Adsorption kinetic models for adsorption of Pb^{2+} on CHE capped M/PU/Si NC: (a) PFO, (b) PSO, (c) IPD. Adsorption conditions were at pH=5, C_0=100 mg·L^{-1}, adsorbent dose=2 g·L^{-1}, agitation speed=200 r·min^{-1}, T=25 °C).

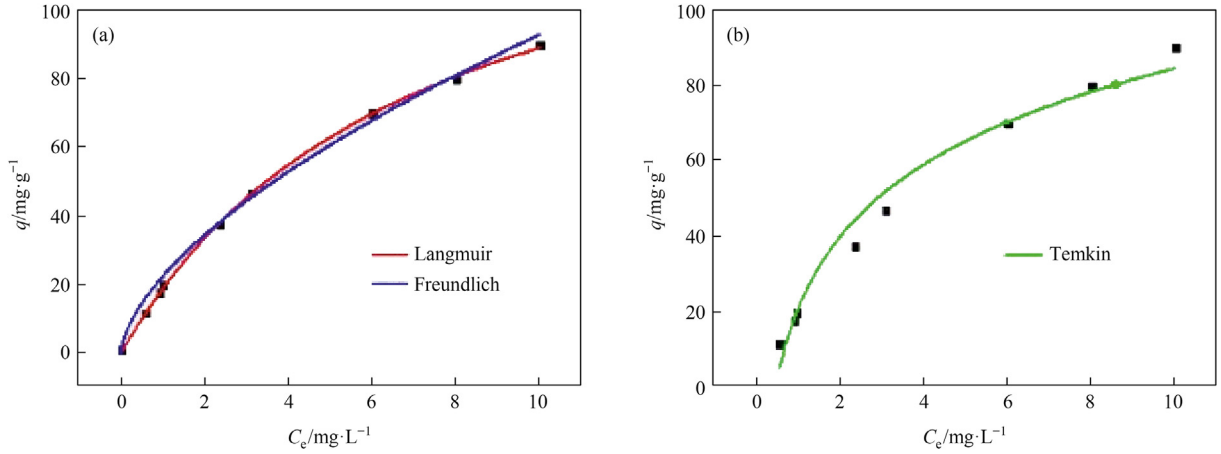

Fig. 13. (a) Langmuir and Freundlich adsorption isotherm. (b) Temkin adsorption Isotherm. Adsorption conditions were at pH=5, t=60 min, speed=200 r·min^{-1}, adsorbent dose=2 g·L^{-1}.

even in the presence of competing ions, indicating minimal competitive interference.

3.6. Reusability of CHE capped M/PU/Si-NC

Reusability of adsorbents is a key component of their economic viability, determining production costs. As a result, determining the reusability of adsorbent materials is critical. The spent CHE-capped M/PU/Si-NC adsorbent was regenerated with 5% HCl as the desorbing agent [18]. Fig. 15 shows the Pb^{2+} uptake onto CHE-capped M/PU/Si NC for various reuse cycles. The Pb^{2+} uptake was 82, 76, 72, 67, and 64 mg·g^{-1} for the first, second, third, fourth, and fifth reuse cycles. The observed decrease in Pb^{2+} uptake could be attributed to a reduction in adsorbent active sites. As shown in

Table 3
Summary of isotherm model parameters.

Isotherm	q_m/mg·g^{-1}	Parameters	R^2
Langmuir	151	K_L=0.1426 L·mg^{-1}	0.999
Freundlich		K_f=22.66 g·mg^{-1}·min^{-1}, n=1.624	0.991
Temkin		A_t=2.08 L·g^{-1}, b_t = 91.8 kJ·mol^{-1}	0.977

Table 4
Comparison of adsorption capacities of different magnetic silica-based adsorbents for Pb^{2+} removal.

Adsorbent	Adsorption capacity /mg·g^{-1}	Reference
Silica-coated magnetic nanocomposites	14.9	[18]
Magnetic mesoporous silica	143.47	[28]
Magnetic sepiolite/iron(III) oxide composite	90.1	[94]
Magnetite nanoparticles	108.23	[95]
CHE capped M/PU/Si NC	151	This study

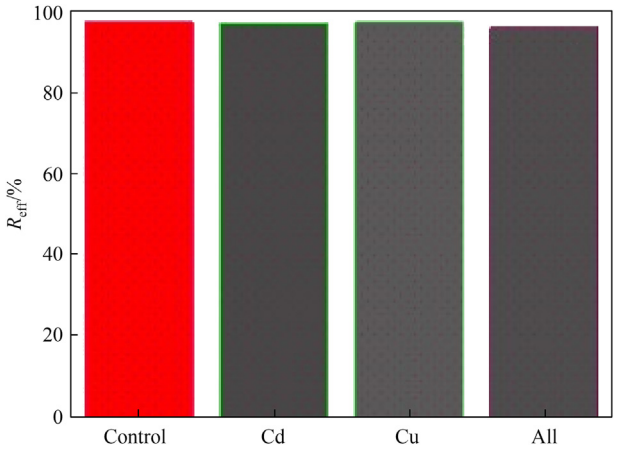

Fig. 14. Effects of competing ions on Pb^{2+} adsorption in aqueous solution (adsorption conditions were C_0=100 mg·L^{-1}, adsorbent dose=2 g·L^{-1}, pH=5, t=60 min, agitation speed = 200 r·min^{-1}, T = 25 °C).

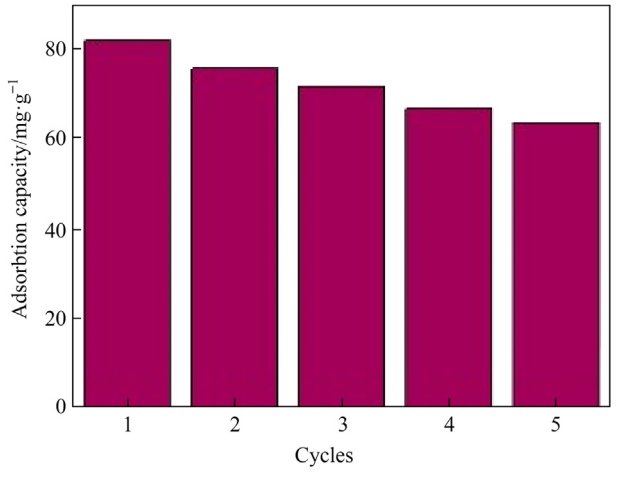

Fig. 15. Regeneration and adsorption capacity of CHE capped M/PU/Si-NC after lead adsorption.

Fig. 15, the CHE-capped M/PU/Si-NC maintained nearly 69.6% of its initial adsorption capacity after five cycles, indicating its excellent recoverability when removing Pb^{2+} from water.

4. Conclusions

In this study, CHE/M/PU/Si-NC was synthesized and applied for the efficient removal of Pb^{2+} ions from aqueous environments. CHE-capped silica NPs synthesized *via* plant-mediated methods exhibit superior thermal stability and a remarkable surface area of 338 m^2·g^{-1}, surpassing that of their sol–gel synthesized counterparts, which demonstrated a surface area of 309 m^2·g^{-1}. Furthermore, the CHE/M/PU/Si-NC emerged as a standout, boasting an extensive surface area alongside a significantly negative surface charge (−37 mV). This unique combination of physical properties renders it exceptionally suitable for adsorbing cationic lead ions. The adsorption capacity remained robust, with Pb^{2+} uptakes recorded at 82.2, 76, 72, 67, and 64 mg·g^{-1} for the first through fifth cycles, respectively. The adsorption efficacy of the CHE/M/PU/Si-NC was rigorously evaluated and found to be in excellent agreement with the Langmuir adsorption isotherm and the PSO kinetic models. This suggests that the silica matrix within the NC, through its silanol (—Si—OH) groups, facilitates the chemisorption and monolayer adsorption of lead ions. The recyclability of the CHE/M/PU/Si-NC adsorbent demonstrated commendable reuse potential across five cycles. The inclusion of magnetic NPs enhanced the post-adsorption separation efficiency and facilitated the recovery and subsequent reuse of the adsorbent material. The demonstrated efficacy of the CHE/M/PU/Si-NC in laboratory conditions paves the way for its application on a larger scale and underscores the need for further studies to evaluate its performance in real-world water treatment scenarios.

CRediT Authorship Contribution Statement

Genet Tsegaye: Writing – review & editing, Writing – original draft, Visualization, Validation, Supervision, Formal analysis, Conceptualization. Zebene Kiflie: Writing – review & editing, Visualization, Validation, Conceptualization. Jemal Fito Nure: Writing – review & editing, Validation, Formal analysis. Abera D. Ambaye: Writing – review & editing, Validation, Formal analysis, Conceptualization.

Declaration of Competing Interest

The authors declare that they have no known competing financial interests or personal relationships that could have appeared to influence the work reported in this paper.

References

[1] J. Briffa, E. Sinagra, R. Blundell, Heavy metal pollution in the environment and their toxicological effects on humans, *Heliyon* 6 (9) (2020) e04691.
[2] M. Rezaei, N. Pourang, A.M. Moradi, Removal of lead from aqueous solutions using three biosorbents of aquatic origin with the emphasis on the affective factors, *Sci. Rep.* 12 (1) (2022) 1–20.
[3] M. Balali-Mood, K. Naseri, Z. Tahergorabi, M.R. Khazdair, M. Sadeghi, Toxic mechanisms of five heavy metals: mercury, lead, chromium, cadmium, and arsenic, *Front. Pharmacol.* 12 (2021) 1–19.
[4] N.A.A. Qasem, R.H. Mohammed, D.U. Lawal, Removal of heavy metal ions from wastewater: a comprehensive and critical review, *npj Clean Water* 4 (1) (2021) 1–15.
[5] S.U. Khan, M. Khalid, K. Hashim, M.H. Jamadi, Efficacy of electrocoagulation treatment for the abatement of heavy metals: an overview of critical processing factors, kinetic models and cost analysis, *Sustain. Times* 15 (2) (2023) 15021708.
[6] F. Gholami, A. Asadi, A.A. Zinatizadeh, Efficient heavy metals and salts rejection using a novel modified polysulfone nanofiltration membrane, *Appl. Water Sci.* 12 (7) (2022) 1–18.
[7] M. Agarwal, K. Chaudhry, Heavy metal sources impacts & removal technologies, *Inter J. Eng. Sci.* 3 (3) (2015) 1–7.
[8] A.E. Burakov, E.V. Galunin, I.V. Burakova, A.E. Kucherova, Adsorption of heavy metals on conventional and nanostructured materials for wastewater treatment purposes: a review, *Ecotoxicol. Environ. Saf.* 148 (2018) 702–712.

[9] R. Baby, M.Z. Hussein, A.H. Abdullah, Z. Zainal, Nanomaterials for the treatment of heavy metal contaminated water, *Polymers* 14 (3) (2022) 1–17.
[10] Z.H. Mohammad, F. Ahmad, S.A. Ibrahim, S. Zaidi, Application of nanotechnology in different aspects of the food industry, *Discov. Food* 2 (1) (2022).
[11] I. Ijaz, E. Gilani, A. Nazir, A. Bukhari, Detail review on chemical, physical and green synthesis, classification, characterizations and applications of nanoparticles, *Green Chem. Lett. Rev.* 13 (3) (2020) 59–81.
[12] P. Samaddar, Y.S. Ok, K.H. Kim, E.E. Kwon, D.C.W. Tsang, Synthesis of nanomaterials from various wastes and their new age applications, *J. Clean. Prod.* 197 (2018) 1190–1209.
[13] H. Sadegh, G.A.M. Ali, V.K. Gupta, A.S.H. Makhlouf, R. Shahryari-ghoshekandi, M. N. Nadagouda, M. Sillanpää, E. Megiel, The role of nanomaterials as effective adsorbents and their applications in wastewater treatment, *J. Nanostruct Chem.* 7 (2017) 1–14.
[14] M. Irfan, A. Arif, M.A. Munir, M.Y. Naz, S. Shukrullah, Statistically analyzed Heavy metal removal efficiency of silica- treatment, *ACS Omega* 28 (3) (2023) 447–452.
[15] Z. Raji, A. Karim, A. Karam, S. Khalloufi, Adsorption of heavy metals: mechanisms, kinetics, and applications of various adsorbents in wastewater remediation—A review, *Waste* 1 (3) (2023) 775–805.
[16] L. Spitzmüller, F. Nitschke, B. Rudolph, J. Berson, T. Schimmel, T. Kohl, Dissolution control and stability improvement of silica nanoparticles in aqueous media, *J. Nanoparticle Res.* 25 (3) (2023)ARTN 40.
[17] A. Taufiq, A. Nikmah, A. Hidayat, S. Sunaryono, Synthesis of magnetite/silica nanocomposites from natural sand to create a drug delivery vehicle, *Heliyon* 6 (2020) e03784.
[18] R. Nicola, O. Costişor, M. Ciopec, A. Negrea, R. Lazău, Silica-coated magnetic nanocomposites for Pb^{2+} removal from aqueous solution, *Appl. Sci.* 10 (8) (2020) 10082726.
[19] M. Irfan, A. Arif, M.A. Munir, M.Y. Naz, Statistically analyzed heavy metal removal efficiency of silica-coated $Cu_{0.50}Mg_{0.50}Fe_2O_4$ magnetic adsorbent for wastewater treatment, *ACS Omega* 8 (50) (2023) 47623–47634.
[20] N. Ahmad, H. Sereshti, M. Mousazadeh, H. Rashidi Nodeh, M.A. Kamboh, S. Mohamad, New magnetic silica-based hybrid organic-inorganic nanocomposite for the removal of lead(II) and nickel(II) ions from aqueous solutions, *Mater. Chem. Phys.* 226 (Ii) (2019) 73–81.
[21] Y. Xu, Y. Li, Z. Ding, Network–polymer–modified superparamagnetic magnetic silica nanoparticles for the adsorption and regeneration of heavy metal ions, *Molecules* 28 (21) (2023) 28217385.
[22] V.P. Aswathi, S. Meera, C.G.A. Maria, M. Nidhin, Green synthesis of nanoparticles from biodegradable waste extracts and their applications: A critical review, *Nanotechnol. Environ. Eng.* 8 (2) (2023) 377–397.
[23] Y.H. Gonfa, F.B. Tessema, A. Bachheti, N. Rai, Anti-inflammatory activity of phytochemicals from medicinal plants and their nanoparticles: A review, *Curr. Res. Biotechnol.* 6 (2023) 100152.
[24] J. Singh, T. Dutta, K.H. Kim, M. Rawat, P. Samddar, P. Kumar, Green' synthesis of metals and their oxide nanoparticles: Applications for environmental remediation, *J. Nanobiotechnol.* 16 (1) (2018) 1–24.
[25] A.M. Atta, Y.M. Moustafa, A.O. Ezzat, A.I. Hashem, Novel magnetic silica-ionic liquid nanocomposites for wastewater treatment, *Nanomaterials* 10 (1) (2020) 1–19.
[26] F. Dadvar, D. Elhamifar, Magnetic silica/graphene oxide nanocomposite supported ionic liquid–manganese complex as a powerful catalyst for the synthesis of tetrahydrobenzopyrans, *Sci. Rep.* 13 (1) (2023) 1–13.
[27] R.G. Digigow, J.F. Dechézelles, H. Dietsch, Preparation and characterization of functional silica hybrid magnetic nanoparticles, *J. Magn. Magn Mater.* 362 (2014) 72–79.
[28] Y. Liang, Z. Han, Q. Zeng, S. Wang, W. Sun, Effective removal of Pb^{2+} from aqueous solution using magnetic mesoporous silica prepared by rubidium-containing biotite leaching residues and wastewater, *Water (Switzerland)* 14 (17) (2022) 2652.
[29] G. Falk, G.P. Shinhe, L.B. Teixeira, E.G. Moraes, A.P.N. de Oliveira, Synthesis of silica nanoparticles from sugarcane bagasse ash and nano-silicon *via* magnesiothermic reactions, *Ceram. Int.* 45 (17) (2019) 21618–21624.
[30] S. Rovani, J.J. Santos, P. Corio, D.A. Fungaro, An alternative and simple method for the preparation of bare silica nanoparticles using sugarcane waste ash, an abundant and despised residue in the Brazilian industry, *J. Braz. Chem. Soc.* 30 (7) (2019) 1524–1533.
[31] P. Worathanakul, P. Mothong, P. Engkawara, Fe_2O_3-SiO_2 nanocomposite derived from bagasse ash for Cr(VI) removal, *J. Biobased Mater. Bioenergy* 7 (2) (2013) 219–222.
[32] D. Dhaneswara, A. Tsania, J.F. Fatriansyah, A. Federico, Synthesis of mesoporous silica from sugarcane bagasse as adsorbent for colorants using cationic and non-ionic surfactants, *Int. J. Technol.* 15 (2) (2024) 373–382.
[33] E.M. Papaslioti, P. Le Bouteiller, H. Carreira, J.M. Greneche, A. Fernandez-Martinez, L. Charlet, Immobilisation of contaminants by 'green'-synthesized magnetite as a remediation approach to the phosphogypsum waste leachates model solution, *J. Environ. Manag.* 341 (2023) 117997.
[34] S. Karina, A.W. Perdana, V. Prajaputra, N. Isnaini, P.H. Nuufus, A. Bismi, Silica-magnetite composite as an eco-friendly adsorbent for aqueous tetracycline removal – kinetic and isotherm studies, *Ecol. Eng. Environ. Technol.* 25 (1) (2024) 82–92.
[35] M.B. Aregu, S.L. Asfaw, M.M. Khan, Identification of two low-cost and locally available filter media (pumice and scoria) for removal of hazardous pollutants from tannery wastewater, *Environ. Syst. Res.* 7 (1) (2018) 1186.
[36] X. Wang, D. Li, R. Bai, S. Liu, C. Yan, J. Zhang, Evolution of the pore structure of pumice aggregate concrete and the effect on compressive strength, *Rev. Adv. Mater. Sci.* 62 (1) (2023) 1515.
[37] L.A. September, N. Kheswa, N.S. Seroka, L. Khotseng, Green synthesis of silica and silicon from agricultural residue sugarcane bagasse ash - A mini review, *RSC Adv.* 13 (2) (2023) 1370–1380.
[38] G. Tsegaye, Z. Kiflie, T.H. Mekonnen, M. Jida, Synthesis and characterization of coffee husk extract (CHE)-capped Fe_3O_4/PU/ZnO nanocomposites with antimicrobial activity, *Biomass Convers. Biorefinery* 24 (1) (2024) 0123456789.
[39] M.Z.H. Soleimani, A. Mahvi, H. Amir, K. Yaghmaeian, A. Abbasnia, K. Sharafi, M. Alimohammadi, Effect of modification by five different acids on pumice stone as natural and low-cost adsorbent for removal of humic acid from aqueous solutions - Application of response surface methodology, *J. Mol. Liq.* 290 (2019) 111181.
[40] E. Akhayere, A. Vaseashta, D. Kavaz, Novel magnetic nano silica synthesis using barley husk waste for removing petroleum from polluted water for environmental sustainability, *Sustain. Times* 12 (24) (2020) 22410646.
[41] J.A. Flood-Garibay, M.A. Méndez-Rojas, Synthesis and characterization of magnetic wrinkled mesoporous silica nanocomposites containing Fe_3O_4 or $CoFe_2O_4$ nanoparticles for potential biomedical applications, *Colloids Surfaces A Physicochem. Eng. Asp.* 615 (2021) 126236.
[42] N. Meky, E. Salama, M.F. Soliman, S.G. Naeem, M. Ossman, M. Elsayed, Synthesis of nano-silica oxide for heavy metal decontamination from aqueous solutions, *Water, Air, Soil Pollut.* 235 (2) (2024) 1–23.
[43] E.D. Revellame, D.L. Fortela, W. Sharp, R. Hernandez, M.E. Zappi, Adsorption kinetic modeling using pseudo-first order and pseudo-second order rate laws: A review, *Clean. Eng. Technol.* 1 (2020) 100032.
[44] S. Mustapha, D.T. Shuaib, M.M. Ndamitso, M.B. Etsuyankpa, A. Sumaila, Adsorption isotherm, kinetic and thermodynamic studies for the removal of Pb(II), Cd(II), Zn(II) and Cu(II) ions from aqueous solutions using Albizia lebbeck pods, *Appl. Water Sci.* 9 (6) (2019) 1–11.
[45] A. Tebeje, Z. Worku, T.T.I. Nkambule, J. Fito, Adsorption of chemical oxygen demand from textile industrial wastewater through locally prepared bentonite adsorbent, *Int. J. Environ. Sci. Technol.* 19 (3) (2022) 1893–1906.
[46] S. Kalam, S.A. Abu-Khamsin, M.S. Kamal, S. Patil, Surfactant adsorption isotherms: A review, *ACS Omega* 6 (48) (2021) 32342–32348.
[47] S. Shamohammadi, M. Khajeh, R. Fattahi, M. Kadkhodahosseini, Introducing the new model of chemical adsorption for heavy metals by Jacobi activated carbon adsorbents, Iranian activated carbon and blowy sand, *Case Stud. Chem. Environ. Eng.* 6 (2022) 100220.
[48] K.H. Chu, Revisiting the Temkin isotherm: dimensional inconsistency and approximate forms, *Ind. Eng. Chem. Res.* 60 (35) (2021) 13140–13147.
[49] R. Seyoum, B.B. Tesfamariam, D.M. Andoshe, A. Algahtani, G.M.S. Ahmed, V. Tirth, Investigation on control burned of bagasse ash on the properties of bagasse ash-blended mortars, *Materials* 14 (17) (2021) 14174991.
[50] P. Chindaprasirt, U. Rattanasak, Eco-production of silica from sugarcane bagasse ash for use as a photochromic pigment filler, *Sci. Rep.* 10 (1) (2020) 1–8.
[51] S.P. Singh, N. Endley, Fabrication of Nano-Silica from Agricultural Residue and Their Application, INC, 2020.
[52] W.K. Setiawan, K.Y. Chiang, Crop residues as potential sustainable precursors for developing silica materials: A review, *Waste and Biomass Valorization* 12 (5) (2021) 2207–2236.
[53] S. Rovani, J.J. Santos, P. Corio, D.A. Fungaro, Highly pure silica nanoparticles with high adsorption capacity obtained from sugarcane waste ash, *ACS Omega* 3 (3) (2018) 2618–2627.
[54] Munasir, A.S. Dewanto, A. Yulianingsih, I.K.F. Saadah, Composites of Fe_3O_4/SiO_2 from natural material synthesized by Co-precipitation method, *IOP Conf. Ser. Mater. Sci. Eng.* 202 (1) (2017) 012057.
[55] N.S. Seroka, R. Taziwa, L. Khotseng, Green synthesis of crystalline silica from sugarcane bagasse ash: physico-chemical properties, *Nanomaterials* 12 (13) (2022) 12132184.
[56] P. Wongsa, P. Phatikulrungsun, S. Prathumthong, FT-IR characteristics, phenolic profiles and inhibitory potential against digestive enzymes of 25 herbal infusions, *Sci. Rep.* 12 (1) (2022) 1–11.
[57] G. Tsegaye, Z. Kiflie, T.H. Mekonnen, M. Jida, Synthesis and characterization of coffee husk extract (CHE)- capped ZnO nanoparticles and their antimicrobial activity, *Biomass Convers. Biorefinery* 12 (2) (2023) 0123456789.
[58] R. Kamila, Ridwan, M.P.M. Akhir, A. Patriati, A. Insani, Synthesis of silica particles through conventional sol-gel and sonochemistry methods and the effect of catalyst, water concentration and sample environment to the particle size, *J. Phys. Conf. Ser.* 2193 (1) (2022) 012044.
[59] S. Steven, E. Restiawaty, Y. Bindar, Routes for energy and bio-silica production from rice husk: A comprehensive review and emerging prospect, *Renew. Sustain. Energy Rev.* 149 (2021) 111329.
[60] K. Panwar, M. Jassal, A.K. Agrawal, In situ synthesis of Ag-SiO_2 Janus particles with epoxy functionality for textile applications, *Particuology* 19 (2015) 107–112.
[61] A. Sadat, I.J. Joye, Peak fitting applied to fourier transform infrared and Raman spectroscopic analysis of proteins, *Appl. Sci.* 10 (17) (2020) 10175918.
[62] D.A. de Freitas, J.A. Barbosa, G. Labuto, R.C.F. Nocelli, E.N.V.M. Carrilho, Removal of the pesticide thiamethoxam from sugarcane juice by magnetic nanomodified activated carbon, *Environ. Sci. Pollut. Res.* 29 (53) (2022) 79855–79865.

[63] C.Y. Rahimzadeh, A.A. Barzinjy, A.S. Mohammed, S.M. Hamad, Green synthesis of SiO_2 nanoparticles from Rhus coriaria L. extract: Comparison with chemically synthesized SiO_2 nanoparticles, *PLoS One* 17 (2022) 0268184.
[64] L. Khouchaf, K. Boulahya, P.P. Das, S. Nicolopoulos, V.K. Kis, J.L. Lábár, Study of the microstructure of amorphous silica nanostructures using high-resolution electron microscopy, electron energy loss spectroscopy, X-ray powder diffraction, and electron pair distribution function, *Materials* 13 (19) (2020) 13194393.
[65] Munasir, A.S. Dewanto, D.H. Kusumawati, N.P. Putri, A. Yulianingsih, I.K.F. Sa'Adah, Structure analysis of Fe_3O_4@SiO_2 core shells prepared from amorphous and crystalline SiO2 particles, *IOP Conf. Ser. Mater. Sci. Eng.* 367 (1) (2018) 012010.
[66] A. Ali, Y.W. Chiang, R.M. Santos, X-ray diffraction techniques for mineral characterization: A review for engineers of the fundamentals, applications, and research directions, *Minerals* 12 (2) (2022) 12020205.
[67] D. Chen, T. Awut, B. Liu, Y. Ma, T. Wang, I. Nurulla, Functionalized magnetic Fe_3O_4 nanoparticles for removal of heavy metal ions from aqueous solutions, *E-Polymers* 16 (4) (2016) 313–322.
[68] N. Sheth, D. Ngo, J. Banerjee, Y. Zhou, C.G. Pantano, S.H. Kim, Probing hydrogen-bonding interactions of water molecules adsorbed on silica, sodium calcium silicate, and calcium aluminosilicate glasses, *J. Phys. Chem. C* 122 (31) (2018) 17792–17801.
[69] N. Wei, M.X. Wei, B.H. Huang, X.F. Guo, H. Wang, One-pot facile synthesis of green-emitting fluorescent silicon quantum dots for the highly selective and sensitive detection of nitrite in food samples, *Dyes Pigments* 184 (2021) 108848.
[70] T. Liu, Y. Pang, X. Xie, W. Qi, Y. Wu, Synthesis of microporous Ni/NiO nanoparticles with enhanced microwave absorption properties, *J. Alloys Compd.* 667 (2016) 287–296.
[71] K. Faaliyan, H. Abdoos, E. Borhani, S.S.S. Afghahi, Magnetite-silica nanoparticles with core-shell structure: Single-step synthesis, characterization and magnetic behavior, *J. Sol. Gel Sci. Technol.* 88 (3) (2018) 609–617.
[72] O. Kapusta, A. Zeleňáková, P. Hrubovčák, V. Girman, V. Zeleňák, Fe_2O_3 and Gd_2O_3 nanoparticles embedded in mesoporous silica: Magnetic properties comparison 131 (4) (2017) 860–862.
[73] E.N. Bakatula, D. Richard, C.M. Neculita, G.J. Zagury, Determination of point of zero charge of natural organic materials, *Environ. Sci. Pollut. Resear* 8 (2018) 1–11.
[74] A. Mahtabani, I. Rytöluoto, R. Anyszka, X. He, E. Saarimäki, K. Lahti, On the silica surface modification and its effect on charge trapping and transport in PP-based dielectric nanocomposites, *ACS Appl. Polym. Mater.* 2 (8) (2020) 3148–3160.
[75] H. Tabasi, M.T.H. Mosavian, M. Darroudi, M. Khazaei, A. Hashemzadeh, Z. Sabouri, Synthesis and characterization of amine-functionalized Fe_3O_4/Mesoporous Silica Nanoparticles (MSNs) as potential nanocarriers in drug delivery systems, *J. Porous Mater.* 29 (6) (2022) 1817–1828.
[76] S. Wonorahardjo, F. Fajaroh, R. Joharmawan, N. Nazriati, E. Budiasih, Cadmium and lead ions adsorption on magnetite, silica, alumina, and cellulosic materials, *Sci. Rep.* 13 (1) (2023) 1–15.
[77] S. Beisl, R. Herrera Díaz, J. Maroušek, A. Marousková, R. Periakaruppan, Silica nanoparticles from coir pith synthesized by acidic sol-gel method improve germination economics, *Polymers* 14 (2) (2022) 4020266.
[78] S. Torgbo, P. Sukyai, Fabrication of microporous bacterial cellulose embedded with magnetite and hydroxyapatite nanocomposite scaffold for bone tissue engineering, *Mater. Chem. Phys.* 237 (2019) 121868.
[79] S.S.U. Rahman, M.T. Qureshi, K. Sultana, W. Rehman, Single step growth of iron oxide nanoparticles and their use as glucose biosensor, *Results Phys.* 7 (2017) 4451–4456.
[80] L. Lemma, Z. Kiflie, S.K. Kassahun, Adsorption of Pb^{2+} and Cd^{2+} on the l-cysteine-functionalized graphene oxide/chitosan/polyvinyl alcohol hydrogel: kinetic, isotherm, and thermodynamic study, *Remediation* 33 (3) (2023) 233–248.
[81] S.C. Ma, Z.G. Wang, J.L. Zhang, D.H. Sun, G.X. Liu, Detection analysis of surface hydroxyl active sites and simulation calculation of the surface dissociation constants of aqueous diatomite suspensions, *Appl. Surf. Sci.* 327 (2015) 453–461.
[82] A.L. Obsa, N.T. Shibeshi, E. Mulugeta, G.A. Workeneh, Bentonite/amino-functionalized cellulose composite as effective adsorbent for removal of lead: Kinetic and isotherm studies, *Results Eng* 21 (2024) 101756.
[83] I.H. Ifijen, A.B. Itua, M. Maliki, C.O. Ize-Iyamu, S.O. Omorogbe, A.I. Aigbodion, E. U. Ikhuoria, The removal of nickel and lead ions from aqueous solutions using green synthesized silica microparticles, *Heliyon* 6 (9) (2020) e04907.
[84] J. Li, X. Dong, X. Liu, X. Xu, W. Duan, Comparative study on the adsorption characteristics of heavy metal ions by activated carbon and selected natural adsorbents, *Sustain. Times* 14 (23) (2022) 142315579.
[85] A.K. Kushwaha, N. Gupta, M.C. Chattopadhyaya, Adsorption behavior of lead onto a new class of functionalized silica gel, *Arab. J. Chem.* 10 (2017) S81–S89.
[86] Q. Li, W. Shi, Q. Yang, Polarization induced covalent bonding: A new force of heavy metal adsorption on charged particle surface, *J. Hazard Mater.* 412 (2021) 125168.
[87] E. Lemma, Z. Kiflie, S.K. Kassahun, Adsorption of Cr (VI) ion from aqueous solution on acrylamide–grafted starch (Coccinia abyssinicca)–PVA/PVP/chitosan/graphene oxide blended hydrogel: Isotherms, kinetics, and thermodynamics studies, *Separ. Sci. Technol.* 58 (2) (2023) 241–256.
[88] N. Kasera, P. Kolar, S.G. Hall, Nitrogen-doped biochars as adsorbents for mitigation of heavy metals and organics from water: A review, *Biochar* 4 (1) (2022) 906–935.
[89] D. Brahma, H. Saikia, Synthesis of ZrO2/MgAl-LDH composites and evaluation of its isotherm, kinetics and thermodynamic properties in the adsorption of Congo red dye, *Chem. Thermodyn. Therm. Anal.* 7 (2022) 100067.
[90] N. Ayawei, A.N. Ebelegi, D. Wankasi, Modelling and interpretation of adsorption isotherms, *J. Chem.* 2017 (2017) 3039817.
[91] F. Togue Kamga, Modeling adsorption mechanism of paraquat onto Ayous (Triplochiton scleroxylon) wood sawdust, *Appl. Water Sci.* 9 (1) (2019) 1–7.
[92] O.D. Agboola, N.U. Benson, Physisorption and chemisorption mechanisms influencing micro (nano) plastics-organic chemical contaminants interactions: a review, *Front. Environ. Sci.* 9 (2021) 1–27.
[93] S. Tamjidi, B.K. Moghadas, H. Esmaeili, F. Shakerian Khoo, G. Gholami, M. Ghasemi, Improving the surface properties of adsorbents by surfactants and their role in the removal of toxic metals from wastewater: a review study, *Process Saf. Environ. Prot.* 148 (2021) 775–795.
[94] O. Uygun, A. Murat, G.Ö. Çakal, Magnetic sepiolite/iron(III) oxide composite for the adsorption of lead(II) ions from aqueous solutions, *Clay Miner.* 58 (3) (2023) 267–279.
[95] P.B. Hassan, R.O. Rasheed, K. Zargoosh, Cadmium and lead removal from aqueous solution using magnetite nanoparticles biofabricated from portulaca oleracea leaf extract, *J. Nanomater.* 2022 (2022) 1024554.
[96] A. Lolasa, N.T. Shibeshi, E. Mulugeta, A green composite of sodium carboxymethyl cellulose and amino-decorated cellulose reinforced with modified bentonite for removal of lead (II): Kinetics and isotherm studies, *Mater. Today Commun.* 41 (2024) 110412.
[97] M. Kajeiou, A. Alem, S. Mezghich, N.-D. Ahfir, M. Mignot, C. Devouge-Boyer, A. Pantet, Competitive and non-competitive zinc, copper and lead biosorption from aqueous solutions onto flax fibers, *Chemosphere* 260 (33) (2020) 127505.